The Journal of Antibiotics (2022) 75:635–649
https://doi.org/10.1038/s41429-022-00564-0

Japan Antibiotics Research Association
The Society for Actinomycetes Japan

ARTICLE

Antibacterial properties and in silico modeling perspective of nano ZnO transported oxytetracycline-Zn^{2+} complex $[ZnOTc]^{+}$ against oxytetracycline-resistant *Aeromonas hydrophila*

Dhruba Jyoti Sarkar[1] · Debasmita Mohanty[2] · Subhashree Subhasmita Raut[2] · Basanta Kumar Das[1]

Received: 26 April 2022 / Revised: 27 August 2022 / Accepted: 3 September 2022 / Published online: 20 September 2022

Abstract

Emergence of antibiotics resistance has threatening consequences not only for human health but also for animal health issues in agriculture. Several animal pathogenic bacteria have developed antibiotic resistance and managing same has tremendous cost repercussions and may lead to total harvest loss. Hence in the present study, efforts are made to revitalize an old antibiotic molecule, oxytetracycline (OTc), through nanodelivery approaches using zinc oxide nanoparticles (nZnO) to confront OTc resistant fish pathogenic bacteria *Aeromonas hydrophila*. OTc was impregnated in nZnO through in situ precipitation method to develop OTc loaded ZnO nanoparticles (OTc@nZnO) with average size of 99.42 nm. Spectroscopic investigation of same revealed complexation of Zn^{2+} with amide and aromatic carbonyl moieties of OTc $[ZnOTc]^{+}$. The complex performed better against *A. hydrophila* with 7–15 mm inhibition zone as compared to nil for bare OTc at same dose. OTc also showed MIC of 150 μg ml^{-1} and for OTc@nZnO it was 7.02 μg ml^{-1} with faster killing rate (k, −0.95). In silico docking simulation suggest that $[ZnOTc]^{+}$ had low binding affinity (LBE > −5.00 kcal mol^{-1}) toward TetR(E) and TetA(E) proteins of *A. hydrophila* as compared to OTc (LBE < −8.00 kcal mol^{-1}). This study postulates that $[ZnOTc]^{+}$ released from OTc@nZnO can escape TetR(E) and TetA(E) resistance proteins and bind at 30S ribosomal subunit with high affinity (<−11.00 kcal mol^{-1}) to exert antibacterial properties. In the recent scenario of recurrent antimicrobial resistance, the develop antibiotic-nanocomposites could come out as potential solution, however further study is required for its feasibility for use in animal health care.

Introduction

Occurrence of antimicrobial resistance is a worldwide menace posing threat not only to human health, but also hampering agricultural production system by developing resistant pathogenic bacterial strains which are difficult to manage by using conventional antibiotics like tetracyclines (Tc). Tc are used widely for treatment of farm animal diseases. For example, respiratory disease (BRD) [1] and digital dermatitis [2] in bovine, enteric red mouth [3], vibriosis [4] and bacterial hemorrhagic septicemia [5] in fishes, etc. In the bacteria, Tc binds to the 30S ribosomal subunit and inhibits the protein synthesis by blocking the binding of aminoacylated tRNA to the A site [6]. However, recently there are many reports from the agricultural farms on development of bacterial resistance against Tc. For example, occurrence of Tc resistant *Pasteurella multocida* (83%) causing BRD [7], *Anaplasma* species causing acute anaplamosis in cattle and sheep [8], fish pathogenic bacteria in mariculture [9–11], etc.

Tc resistance in pathogenic bacteria is caused by introduction of Tc resistance genes producing proteins responsible for binding-site alteration/ribosomal protection, efflux pump, enzymatic degradation, etc. [12, 13]. However, in gram negative bacteria it is primarily due to active transport of drug out of the bacterial cell by intrinsic membrane transport protein TetA [14]. TetA protein acts as an

Supplementary information The online version contains supplementary material available at https://doi.org/10.1038/s41429-022-00564-0.

✉ Basanta Kumar Das
basantakumard@gmail.com

[1] Aquatic Environmental Biotechnology and Nanotechnology Division, ICAR-Central Inland Fisheries Research Institute, Barrackpore, Kolkata 700120, India

[2] Riverine and Estuarine Fisheries Division, ICAR-Central Inland Fisheries Research Institute, Barrackpore, Kolkata 700120, India

antiporter across the membrane and facilitates the efflux of Tc divalent cation complex $[MgTc]^+$ out of the cell. However, the expression of TetA is highly controlled by the Tet repressor (TetR) protein which is having very high affinity (K_A ~10^9 M^{-1}) toward Tc [15]. TetR also regulates transcription of its own gene tetR and upon binding to $[MgTc]^+$ it changes its conformation that cannot regulates transcription of both tetR and tetA. As a result, TetR and the resistance protein TetA are expressed which exports the antibiotics out of cell before inhibition of protein synthesis. TetR is a homodimer α-helix-turn- α-helix sequence motif and folds in to 10 α helices (α1 to α10) with connecting turns and loops [15, 16]. Tc binding pocket of TetR is composed of COOH-termini of α4 and α6 and the helices α5, α7, α8, α8', α9' [16]. Hence it was hypothesized that a change in the conformation of Tc can alter the binding affinity toward TetR and also improves the inhibition of protein synthesis by binding the ribosome.

In the present study molecular conformation of a model Tc antibiotics i.e. oxytetracycline (OTc) was changed by introducing Zn^{2+} as divalent cation and further zinc oxide nanoparticles (nZnO) was used as carrier of the complex $[ZnOTc]^+$ so that the it has lower binding affinity toward TetR and bypass the efflux mechanism. Previously, a few studies reported improvement of antibacterial properties of drug molecule in association with Zn^{2+} and ZnO. For example, a combination of OTc and ZnO loaded on to polycaprolactone nanofibers showed excellent activity against a mixed bacterial culture with 97.5% growth inhibition [17]. Similarly, a recent clinical study reported that a combination of Zn and Tc antibiotics showed better bacteriacidal effect toward multidrug-resistant strains of *Acinetobacter baumannii* isolated from pneumonia affected COVID-19 patients [18]. Use of nanoparticle as carrier for antibiotics have proven as better option to enhance the efficacy of antibiotics and reinvigorate obsolete antibiotics against resistant pathogen [19]. For example, Tc loaded on para-amino benzoic acid functionalized grapheme oxide nanosheets performed better against resistant *Escherichia coli*. [20]. Similarly, loading of Tc into calcium phosphate nanoparticles (8 ± 5 nm) had shown to reduce MIC from 150–180 μg ml^{-1} to 20–40 μg ml^{-1} against resistant strains of *E. coli, Salmonella kentuckey, Shigella flexneri* [21]. Covalently attached ciprofloxacin on Single-walled carbon nanotubes (SWNT) was also found to be 16 times more effective against *Staphylococcus aureus* and *Pseudomonas aeruginosa*, and eight times more effective in case of *E. coli* [22]. SWNT and nanographene oxide was used to deliver Tc to kill *E. coli* with an efflux pump resistance mechanism and found to reduce MIC value from 200 to 38–75 μg ml^{-1} [23].

In the present study the efficacy of $[ZnOTc]^+$ complex loaded on nZnO (OTc@ZnO) was tested against a model gram negative bacterium i.e., *Aeromonas hydrophila* which is a highly prevalent fish pathogenic bacteria and recently, it showed widespread occurrence of resistance [24, 25]. For example, OTc resistance incidences observed in *Aromonas* spp. isolated from *Sparus aurata* reared in Italian mariculture farms [26]. Similarly, a study in Czech carp fisheries found that 41% of isolated *Aeromonas* sp. ($n = 159$) were resistant to OTc [27]. This is first kind of any study where interaction of OTc and Zn^{2+} as a complex $[ZnOTc]^+$ was reported to show breaking of Tc resistance.

Materials and methods

Materials

Oxytetracycline hydrochloride (OTc. HCl) or 5-hydroxytetracycline hydrochloride ($C_{22}H_{24}N_2O_9$. HCl) (95%) was purchased from Sigma-Aldrich. Zinc sulfate heptahydrate ($ZnSO_4.7\ H_2O$) and sodium hydroxide pellet (NaOH) was purchased from Himedia Laboratories Pvt. Ltd. India. For routine work, analytical grade chemicals and solvents were employed.

Synthesis of nZnO and OTC@nZnO

The nZnO was prepared as per previous method with slight modification [28]. Briefly, a solution of $ZnSO_4$ (20 mM) was prepared with MiliQ water (18 Ω) followed by stirring (400 rpm) and drop wise addition of equal volume of NaOH solution (12 mM) to get white suspension (pH recorded at 10.0). The suspension was vigorously stirred for 10 min followed by centrifugation (4000 rpm) to get precipitates. The white precipitates were dried first at 100 °C for 6 h and then calcinations at 300 °C for 1 h followed by grinding to get fine powder.

The complex $[ZnOTc]^+$ loaded on to nZnO (OTc@nZnO) was prepared by mixing $ZnSO_4$ solution (20 mM) with OTc solution (10 mM) while stirring (400 rpm) followed by drop wise addition of NaOH (12 mM) to yield yellowish suspension (pH recorded at 8.0) at dark condition. The suspension was vigorously stirred for 10 min followed by centrifugation (4000 rpm) to get precipitates which was washed three times with MiliQ water. The final suspension was dried in room temperature (29 °C) followed by storing in desiccator at dark.

Characterization of nZnO and OTc@nZnO

The morphology of nZnO and OTC@nZnO were measured by high resolution transmission electron microscope (HRTEM) (JOEL, JEM-2010). The known quantity of dried nZnO and OTC@nZnO were dispersed in MiliQ water following sonication (at 80% amplitude, 25 kHz). The dispersed materials were drop casted on carbon coated copper

grid and analysis was performed in the HRTEM with at an acceleration voltage of 200 kV.

To confirm the loading of OTc on to nZnO, Fourier transformed infra-red (FTIR) spectroscopic analysis was performed. The dried powders of nZnO, OTc and OTc@nZnO were analyzed in ATR FT-IR (Spectrum 100 FTIR Spectrometer, PerkinElmer) and percent absorbance was recorded at range 650–4000 cm^{-1} with a resolution of 1 cm^{-1} [29].

The attachment position of Zn^{2+} on to OTc molecule was identified by comparing absorbance (λ_{max}) values of OTc and $[ZnOTc]^{+}$ using UV-Vis spectrophotometer. The λ_{max} values of OTC was elucidated using Woodward-fieser rule for aromatic carbonyl compounds (D ring) and 6-member cyclic α, β unsaturated ketones (A ring) [30, 31].

Loading and release kinetics

The percent loading of OTc on to nZnO was determined by adding 1 ml Conc. HCl (37%) to 0.01 g OTc@nZnO followed by volume make to 100 ml and measuring absorption at 270 nm using UV-Vis spectrophotometer. The rate of release of $[ZnOTc]^{+}$ from the OTc@nZnO was determined using dialysis method [32]. A known amount of OTc@nZnO was dispersed in MiliQ water using sonication (at 80% amplitude, 25 kHz) for 2 min and was taken in a dialysis bag with 10 kDa membrane. The dialysis bag was dipped in a beaker containing 100 ml phosphate buffer. The set up was maintained for 2 days and at regular interval 2 ml of aliquot was withdrawn from the beaker and the amount of OTc released was estimated using UV-Vis spectrophotometer at 270 nm.

Bacterial strains and antibacterial activity

Bacterial species used in the study was *A. hydrophila* which are abundantly found in the tropical aquatic ecosystems. *A. hydrophila* ATCC 7966 strain was used as sensitive strain to OTC whereas resistant *A. hydrophila* strain CIAHRT_11 (NCBI, MG754418) was isolated from blood and tail of infected *Labeo rohita* fish collected from aquaculture ponds of West Bengal, India.

All the isolates were revived in Tryptic Soy Broth (TSB) (Himedia Laboratories, India) for 18–20 h and incubated at 37 °C. After incubation the bacterial isolates were diluted up to 0.5 McFarland Standards which contains ~1.5×10^8 cfu ml^{-1} of bacterial population. Using the L-shaped spreader, the diluted bacterial suspension was then spread over the Tryptic Soy Agar (TSA) (Himedia Laboratories, India) plate. The experimental samples were loaded in various concentrations on a blank sterile disc (Himedia Laboratories, India) and placed on the agar plate. A 30 µg OTc disc (Himedia Laboratories, India) was also placed in the middle of the plate. Those plates were incubated for 24 h at 37 °C. The inhibition zone of the samples which were loaded on the sterile disc and the OTc disc were measured and recorded after 24 h.

Minimal inhibitory concentration (MIC) and minimum bactericidal concentration (MBC)

MIC is referred as the antimicrobial drug concentration which completely inhibit the growth of bacterial population (~10^6 cells ml^{-1}) occurs during 18–20 h of incubation at 35 ± 2 °C [33]. In the present study overnight grown bacterium culture was inoculated into TSB at final concentration >10^6 cells ml^{-1} which was divided in different parts (2 ml each) to treat with OTc and OTc@nZnO at different concentrations. The treated bacterial cultures were incubated at 35 °C with shaking for 24 h followed by assessment of number of viable bacterial cell through serial dilution and spreading over TSA.

Determination of death rate

The death rate of test bacteria in the presence of OTc and OTc@nZnO was determined to understand the efficacy of developed drug nanomaterial composite. At first overnight grown bacterial cell cultures were ten times diluted in fresh TSB medium followed by incubation to grow (at 35 °C with shaking) up to log phase (~5×10^{10} cells ml^{-1}). The test antimicrobials were then added at MIC and the bacterial cultures were further allowed to incubate at same condition. Culture aliquots were withdrawn at different time intervals (0, 2, 6, 11, 14, 16 and 24 h), serially diluted and spread on TSA plates to assay number of viable cells. The death rate of OTc and OTc@nZnO treated cells was determined from the slope of the plot "Log N_t/N_0 vs. incubation time". Survivor equation was used to describe the change in bacterial population as a function of time [34]:

$$\mathrm{Log}[N/N_o] = -t/D \quad (1)$$

where N denotes bacterial population at time t; N_o indicates initial bacterial population and D (D-value) is the time required for a 1-log cycle reduction in the bacterial population or decimal reduction time. Corresponding equation for reduction of microbial population is first-order kinetic model [21]:

$$\mathrm{Log}[N/N_o] = -k.t \quad (2)$$

where k denotes first-order rate constant. By comparing Eqs. (1) and (2) we can get the expression:

$$k = 2.303/D \quad (3)$$

The rate constant k indicates the date rate of the bacterial cell and D-value signifies the time required to kill 1-log cycle bacterial population.

In silico $[MgOTc]^+$ and $[ZnOTc]^+$ compound preparation

The molecular structures of $[MgOTc]^+$ and $[ZnOTc]^+$ were prepared in the ChemDraw Ultra (CambridgeSoft) and subjected to energy minimization at the Avogadro platform by using universal force field (UFF) with 5000 steps of steepest descent algorithm [35]. UFF was reported to be does well with organometallic compounds [36]. These steps were performed to generate best conformation of these two molecules. After energy minimization and optimization of geometry the $[MgOTc]^+$ and $[ZnOTc]^+$ showed total energy of 676.9 kJ mol^{-1} and 826.17 kJ mol^{-1}, respectively. The distances between coordinating atoms and metal ion in case of $[MgOTc]^+$ ranged between 1.88–2.00 Å and for $[ZnOTc]^+$ it was between 1.89–1.91 Å (Fig. S1).

TetR and TetA sequence retrieve process and protein structure prediction

Amino acid sequence of Tc resistance transcriptional repressor TetR(E) of *A. hydrophila* was collected from NCBI database with accession id: WP_139390343 [14]. By using NCBI BLASTp server we identified crystal structure (PDB ID: 5MRU_A) with respect to the query sequence of test TetR(E) [37]. Based on sequence alignment between the target protein and the template sequence, homology modeling was used for predicting 3D model of the target protein (PDB ID: 5MRU) through MODELER10.1 package, which was further used in molecular docking purpose [38]. DoGSiteScorer in the webserver https://proteins.plus/ was used to detect potential binding site which revealed that TetR(E) has one prominent binding site (P_0) (Fig. S2Ai, ii). The binding pocket P_0 showed volume of 1380.61 $Å^3$ and surface area of 1693.21 $Å^2$ with high druggability score (0.81) (Table S1). The amino acid residues constructing the P_0 binding site are Ala(5), Asn(2), Asp(1), Gln(4), Glu(1), Gly(2), His(3), Ile(5), Leu(10), Lys(1), Met(1), Phe(1), Pro(2), Ser(6), Thr(4) and Val(1) (Table S1). The same binding pocket in TetR(E) was also indicated by CASTp (http://sts.bioe.uic.edu/castp/) (Fig. S2Aiii). Similarly, amino acid sequence of tetracycline resistance protein TetA(E) of *A. hydrophila* was collected from NCBI database with accession id: PKD25314.1. By using NCBI BLASTp server we identified three crystal structures (PDB ID: 6S4M_A, 7BC6_A and 6T1Z_A) with respect to the query sequence of test TetA(E) [37]. The alignment of query protein sequence was done with the identified crystal structures using Phyre2 web platform (397 residues (100%) modeled at >90% confidence) and 3D model for the target protein was obtained. Binding-site analysis using DoGSiteScorer in the webserver https://proteins.plus/ revealed that TetA(E) has four prominent binding sites (P_0, P_1, P_2 and P_3) with druggability score more than 0.73 (Fig. S2Bi, ii) (Table S2). The details of these binding pockets are given in Table S2 which showed that binding pockets, P_0, P_1 and P_2 were having volume and surface area more than the Connolly solvent excluded volume and accessible area of ligand molecules. However, in CASTp, a single binding pocket was observed covering sites of P_0 and P_1 (Fig. S2Biii). SAVeS server (http://nihserver.mbi.ucla.edu/SAVES/) was used to check the stereo chemical quality of TetR(E) and Tet(A) on PROCHECKweb software which generated Ramachandran plot (RP) [39] (Fig. S3).

Ab initio 16S RNA structures prediction of *A. hydrophilla*

Partial sequences of 16S ribosomal RNA gene of *A. hydrophila* CCM 7232 strain (sensitive) (NCBI, NR_043638.1) and *A. hydrophila* strain CIAHRT_11 (NCBI, MG754418) were collected from NCBI database. At first, the secondary structures of 16S ribosomal RNA genes are prepared using mFold platform (http://www.unafold.org/) deltaG in plot file 12.kcl/mole [40]. The secondary structure of the partial sequences of 16S ribosomal RNA genes are presented in the Supplementary File (Figs. S4 and S5). From secondary structure, the tertiary structures were prepared in 3dRNA (Xiao Lab) using Ab initio technique [41, 42]. For CIAHRT_11, a model with 3dRNAscore of 26.54 was selected and for CCM 7232 it was 25.85.

In silico molecular docking studies

Molecular docking is widely used to predict binding affinity of a ligand to a protein chain. In the current work, to investigate the binding of $[ZnOTc]^+$ on to resistance proteins i.e. TetR(E) and TetA(E), and 16S rRNAs, molecular docking was performed by using the Graphical User Interface program of "Autodock 4.2" (Ver. 4.2.6). The software is considered as best suited automatic docking tool for modeling flexible small drug molecules binding to receptor macromolecules [43]. According to a previous study 50% among the 1300 protein–ligand complexes have their top score conformations below 2 Å threshold using Autodock and the correlation between Autodock score and experimental binding affinity data was about 0.27 [44]. Lamarckian Genetic Algorithm (LGA) was used for conformational search to explore binding conformational landscape of $[ZnOTc]^+$ and $[MgOTc]^+$ docked against TetR€ and T€(E) efflux protein of *A. hydrophila*. Before docking, proteins structures and drug chemical structures were prepared by removing water

molecule, assigned Kollman charges each atom of the residues, defining the rotatable bonds, adding partial charges, adding hydrogen atoms to target protein for better interaction. TetR(E) is evaluated with already reported binding pocket [16] with grid size of $32 \times 28 \times 30$ xyz points with center coordinates of −1.099, 8.795, 10.963 (X, Y, Z). Before docking to check the correct binding pose, self-docking was executed between 5A,6-anhydrotetracycline with TetR(E) to see our docking protocol is optimum. During self-docking experiment it was found that the target ligand binds exactly to the site of identified crystal structure (PDB ID: 5MRU_A) with LBE value of −11.13 kcal/mol (Fig. S6 and Table S3). The docking of 5A,6-anhydrotetracycline in the TetR(E) of *A. hydrophila* generated similar binding efficiency (LBE, −11.79 kcal mol^{-1}) with 3 H-bonds (Fig. S6 and Table S3). The RMSD from the reference structure are below 2.0 Å in both the cases (Table S3) indicating adequacy of the binding protocol. LGA was used for docking simulation by setting the initial position, orientation, and torsions of $[ZnOTc]^+$ and $[MgOTc]^+$ ligand molecules in random position. Ten runs of LGA were set to terminate after a maximum of 250,000 energy evaluations for each docking with population size of 150. Since TetA(E) showed a larger binding pocket (Fig. S2Bi–iii) a blind docking was performed with a larger grid size of $56 \times 36 \times 40$ xyz points with center coordinates of −23.393, 12.054, 30.453 (X, Y, Z:). In total, 100 runs of LGA were set to identify the exact binding site from the binding pockets of the macromolecular structure of TetA(E). Similarly, electrostatic grid map of 16S rRNA of *A. hydrophila* CCM 7232 strain was calculated to identify the best binding sites through blind docking with grid size of $126 \times 126 \times 126$ xyz points with center coordinates of 23.83, 114.99, −78.49 (X, Y, Z) and for 16S rRNA of *A. hydrophila* CIAHRT_11 strain it was with grid size of $126 \times 126 \times 126$ points with center coordinates of 245.48, 117.79, −146.10 (X, Y, Z). In total, 100 runs of LGA were set to identify binding site from the most of 16S rRNAs structure. Finally, the best pose was extracted and aligned with the receptor structure with the lowest binding energy for final analysis. The molecular docking results were visualized in the Discovery Studio and PyMol, and the receptor-ligand interactions like H-bond and other non-bonded energies are analyzed in the Ligplot [45].

Data presentation and statistical analysis

The antibiogram data of OTc and OTc@nZnO against sensitive and resistant strains of *A. hydrophila* is presented as box plot (variables distribution with quartiles and outliers) and prepared using JMP Pro 10 software. The bacterial populations at different doses of antibiotics are presented as Log CFU ml^{-1} vs. OTc (μg ml^{-1}) in both contour and linear regression line with good fit (RMSE: 1.51 to 1.92 for OTc and 0.38–0.54 for OTc@nZnO) and prepared using JMP Pro 10 software. The death kinetics data of both the strains of *A. hydrophila* are presented as Log (N_t/N_o) vs. time (hours) against the test antibiotics and kinetic parameters were analyzed in Microsoft Excel.

Results and discussion

Synthesis and characterization of OTc@nZnO

In the present study OTc loaded nZnO (OTc@nZnO) was synthesized with an objective to attach divalent cation Zn^{2+} to the OTc molecule and delivering the same using nZnO to bypass the cellular drug efflux barrier and exert the antibacterial effect to Tc resistant *A. hydrophila* by binding 30S ribosomal subunit. The OTc@nZnO was synthesized by a co-precipitation method in which OTc molecule was added at the stage of formation of ZnO nanoparticles (nZnO). The synthesis protocol is simple, quick and prepare stable dispersion of OTc@nZnO in water. Since Tcs are light and pH sensitive, the synthesis was done in dark condition and the final pH during co-precipitation was kept at pH 8 [46].

Detailed information on the crystal structure of the samples was analyzed through HR-TEM analysis. At lower magnification TEM images revealed that nanoparticles of ZnO were hexagonal in shape (Fig. 1ai) and at higher resolution TEM micrograph depicts the fringes of the spacing 0.29 nm (d spacing) corresponding to (100) ZnO plane (Fig. 1aii). The SAED pattern of nZnO (Fig. 1aiv) revealed the diffraction rings corresponding to (100), (002), (101), (102), (110) and (112) planes of ZnO. Fig. 1aiii shows the size distribution of nZnO analyzed with help of a histogram of 70 particles (range from 42 to 211 nm) and after Gaussian fit the estimated average particle size is 99.42 nm. However, crystal structure analysis using HR-TEM micrograph of OTC@nZnO revealed that the d-spacing value has increased to >0.3 nm in several regions (Fig. 1bii) and the average particle size has reduced to 17.33 nm (range 8.13–32.70 nm) (Fig. 1biii). This observation revealed that introduction of OTc hindered the crystal growth of ZnO making it smaller sized and also distorted the general crystal structure of ZnO as evident from the diffused diffraction rings of OTc@nZnO (Fig. 1biv).

Further, the loading of OTc in the nZnO was confirmed using FT-IR spectroscopy (Fig. 2a). nZnO showed absorption bands at ~3400 cm^{-1} and 1669 cm^{-1} for O-H stretching and bending vibrations, respectively of free H_2O that are absorbed on the surface of nZnO [47]. Distinct bands at ~600 cm^{-1} and 1111 cm^{-1} are attributed to Z-O stretching [47, 48] and Zn-O-H bending [49] vibrations, respectively. The FT-IR spectra of OTc showed characteristics bands at 3377 cm^{-1} and 2924 cm^{-1} assigned to O-H stretching and C-H stretching vibration [50]. The band at

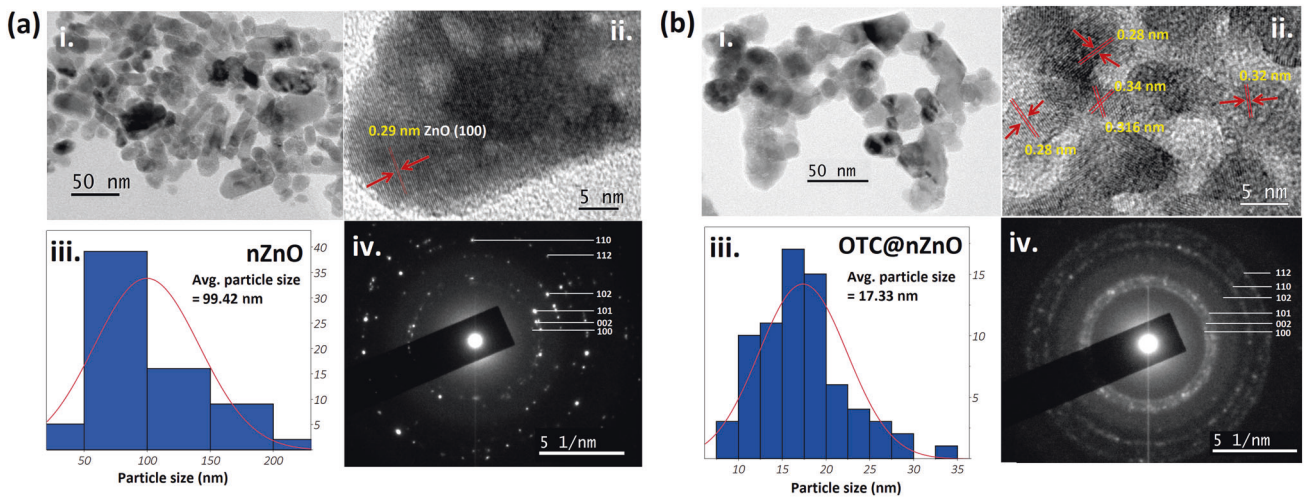

Fig. 1 HR-TEM (i), d spacing (ii), SAED (iii) and particle size distribution (iv) of nZnO (**a**) and OTc@nZnO (**b**)

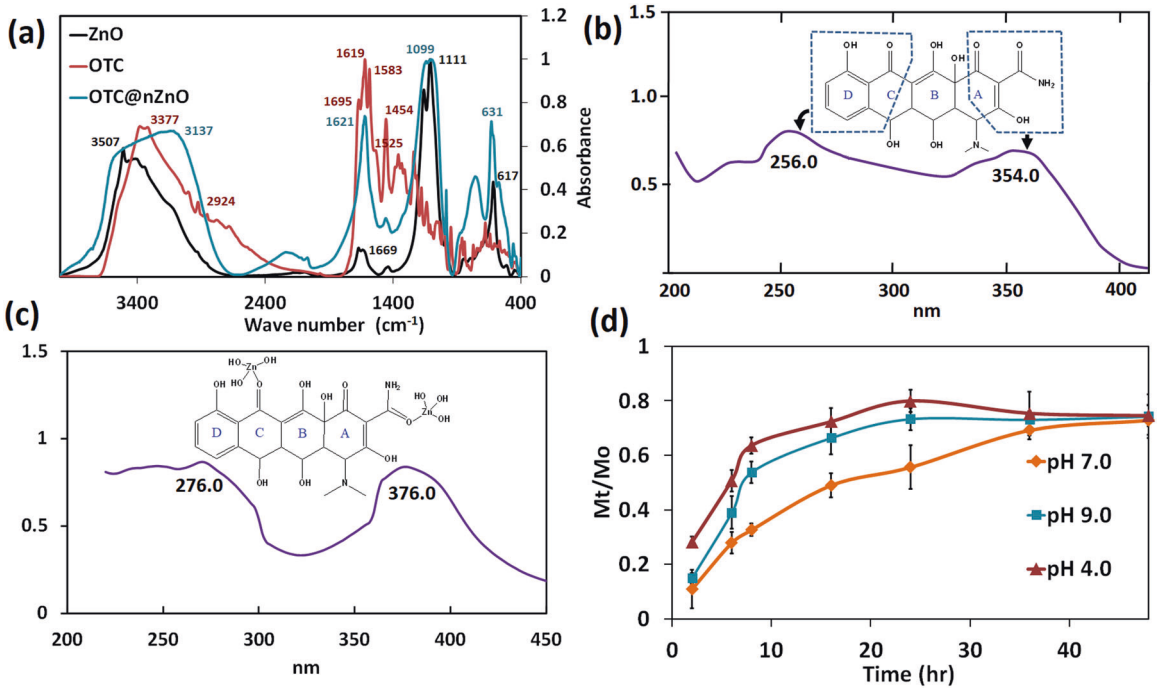

Fig. 2 FT-IR spectra of nZnO, OTc and OTc@nZnO (**a**), UV spectra of OTc (**b**) and OTc@nZnO (**c**); in vitro release kinetics of $[ZnOTc]^+$ from OTc@nZnO (**d**)

1695 cm^{-1} was assigned to C=O stretching vibration of $–CONH_2$ or Amide I and the spectral band for Amide II (N-H bending and C-N stretching) appeared at 1525 cm^{-1} [51]. The C=O stretching vibration of conjugated ketone of ring A appeared at 1619 cm^{-1} whereas C=O of ring C appeared at 1583 cm^{-1} [51]. The spectral band at 1455 cm^{-1} was assigned to aromatic C=C vibration [50]. The FT-IR spectra of OTc@nZnO showed distinct major bands of nZnO and OTc. However, the characteristic spectra at 1695 cm^{-1} because of Amide I and at 1583 cm^{-1} due to >C=O of ring C was absent in OTc@nZnO. Thus, it can be postulated that co-precipitation of nZnO in the presence of OTC has led to complexation of Zn^{2+} in the following two moieties of OTC, (1) the Amide moiety of ring A and (2) >C=O moiety of ring C. Similar observation was also reported in a previous study with interaction of Ca^{2+} in the designated positions of OTc leading to elimination inter-molecular H-bond [21].

To further confirm the complexation nature between Zn^{2+} and OTc, λ_{max} for OTc and OTc@nZnO were observed in the

UV-Vis spectrophotometer. OTc showed two major absorptions peak at 256 and 354 nm (Fig. 2b). Following the Woodward Fieser' rule for correlating λ_{max} with molecular structure, the λ_{max} at 256 nm is assigned to the carbonyl substituted aromatic moiety at ring D and the λ_{max} at 354 nm is assigned to α, β unsaturated carbonyl compound at ring A. The detailed calculation is provided in Table S4. Interestingly, the UV absorbance of OTc@nZnO showed bathochromic or red shift of λ_{max} to 276 nm for aromatic moiety and to 376 nm for α, β unsaturated carbonyl compound (Fig. 2c). Hence, besides the FT-IR spectroscopic results, this bathochromic shift of UV λ_{max} also postulates that Zn^{2+} was complexed with the OTc at ring A and ring D with respective amide and aromatic carbonyl moieties. Previous literature also reports bathochromic shift of OTc from 353.35 to 374 nm due to formation of ligand-to-metal charge transfer coordination compound (LMCT) by OTc molecule in coordination with the d orbitals of the Zn^{2+} [52]. Further, it was extensively reported that Mg^{2+} ion forms coordination compound with Tc molecule near the aromatic moiety at ring D get binds with 16S RNA to block binding of aminoacylated tRNA to the A site. There are extensive reports that the amide group at ring A could bind with various metal ion like Cd, Mo, etc. to form metal coordination compound [53].

Loading and kinetics of $[ZnOTc]^+$ release from OTc@nZnO

Addition of strong acid cause dissolution of metal oxide framework thus releasing the encapsulated drug molecule [54]. In the present study, addition of HCl acid to OTc@nZnO cause complete release of OTc in the water and the same was estimated by measuring absorbance at λ_{max} 270 nm. The calculated OTc loading on to OTc@nZnO was 9.35%. Since the drug molecule must desorb from the zinc oxide crystal framework to exert its antibiotic properties the release of $[ZnOTc]^+$ from the OTc@nZnO suspension was studied and the release data were fitted in to first-order kinetics equation:

$$\frac{M_t}{M_\infty} = \left(\frac{M_t}{M_\infty}\right)_{max} [1 - \exp(-k_f \times t)] \quad (4)$$

where $\frac{M_t}{M_\infty}$ is the fraction of $[ZnOTc]^+$ released at a time t, $\left(\frac{M_t}{M_\infty}\right)_{max}$ stands for the maximum fraction of $[ZnOTc]^+$ released during the total period and k_f denotes first-order rate constant. The in vitro release profile depicted a slow and sustained release of $[ZnOTc]^+$ from OTc@nZnO and 10–28% of the loaded OTc was released with 2 h and more than 0.74% release occurred within 40 h (Fig. 2d). Hence it may be postulated that during in vivo condition, the initial bulk release of drug is sufficient to kill the bacterial cell and subsequent sustained release maintain the killing environment for long duration. It was also found that the rate of release of $[ZnOTc]^+$ was pH dependent and a faster rate was observed at pH 4 and 9 as compared to 7. The higher release rate at pH 4 can be attributed to the dissolution of metal oxide framework of nZnO by presence of HCl. It was reported that ZnO dissolves in water as Zn^{2+} at pH 4 through hydrolysis releasing hydroxyl ions (OH^-) to increase the pH [55]. Though ZnO is fairly stable at alkaline solution, a faster release rate of $[ZnOTC]^+$ at pH 9.0 may be explained by the formation of fairly water-soluble sodium zincate in the presence of NaOH [56]. The release data fitted well to the first-order kinetic equation with high (>0.98) coefficient of determination (R^2) and the rate constant followed the order pH 4 (K_f 0.21) > pH 9 (K_f 0.13) > pH 7 (K_f 0.07) (Table S5).

Antibacterial efficacy, MIC and death kinetics

The antibiogram study (Fig. 3a) revealed that ATCC 7966 strain of *A. hydrophila* is sensitive to both free OTc and OTc@nZnO with similar trend in bacterial zone of inhibition, 17–20 mm and 18.5–22 mm, respectively. However, the *A. hydrophila* strain CIAHRT_11 did not show any zone of inhibition for free OTc at the given dose (30–60 µg). Interestingly, the resistant strain did show a considerable bacterial zone of inhibition (9–16 mm) for OTc@nZnO. Antibiogram studies for synthesized nZnO alone were also done against both the strains, however, no zone of inhibitions was observed (Fig. S7). To better understand the bacteriotoxicity of developed formulation, bacterial cells were exposed to different concentration of free OTc and OTc@nZnO in TSB medium. In case of *A. hydrophila* ATCC 7966 strain, it was observed that free OTc at 50 µg ml^{-1} completely inhibit bacterial cell growth. However, OTc@nZnO exert the same phenomenon at very low concentration of 28.125 µg ml^{-1} which is equivalent to 2.6 µg ml^{-1} OTc (OTc loading 9.35%) (Fig. 3b). Similarly, bacterial population of *A. hydrophila* strain CIAHRT_11 as an effect of various concentration of OTc and OTc@nZnO was also observed (Fig. 3c). Free OTc at 150 µg ml^{-1} concentration could be able to completely inhibit the bacterial population, whereas OTc@nZnO @ 75 µg ml^{-1} (~7.02 µg ml^{-1} OTc) could be able to inhibit bacterial growth. This drastic reduction of MIC was also reported previously where conjugation of silver nanoparticles with methicillin lead to reduction of MIC from 250 to 7.8 µg ml^{-1} against *Staphylococcus epidermidis* [57]. Similarly, conjugation of gentamycin gold nanoparticles led to reduction of MIC from 125 to 31.25 µg ml^{-1} against *S. epidermidis* [58]. In case Tc, nanotization of with calcium phosphate nanoparticles was reported to reduce MIC from 180–150 to 13–35 µg ml^{-1} for multi-drug resistant diarrhea-causing bacteria [21].

Cell death kinetics by free OTc (Fig. 3d) and OTc@nZnO (Fig. 3e) at their MIC concentration revealed that free OTc

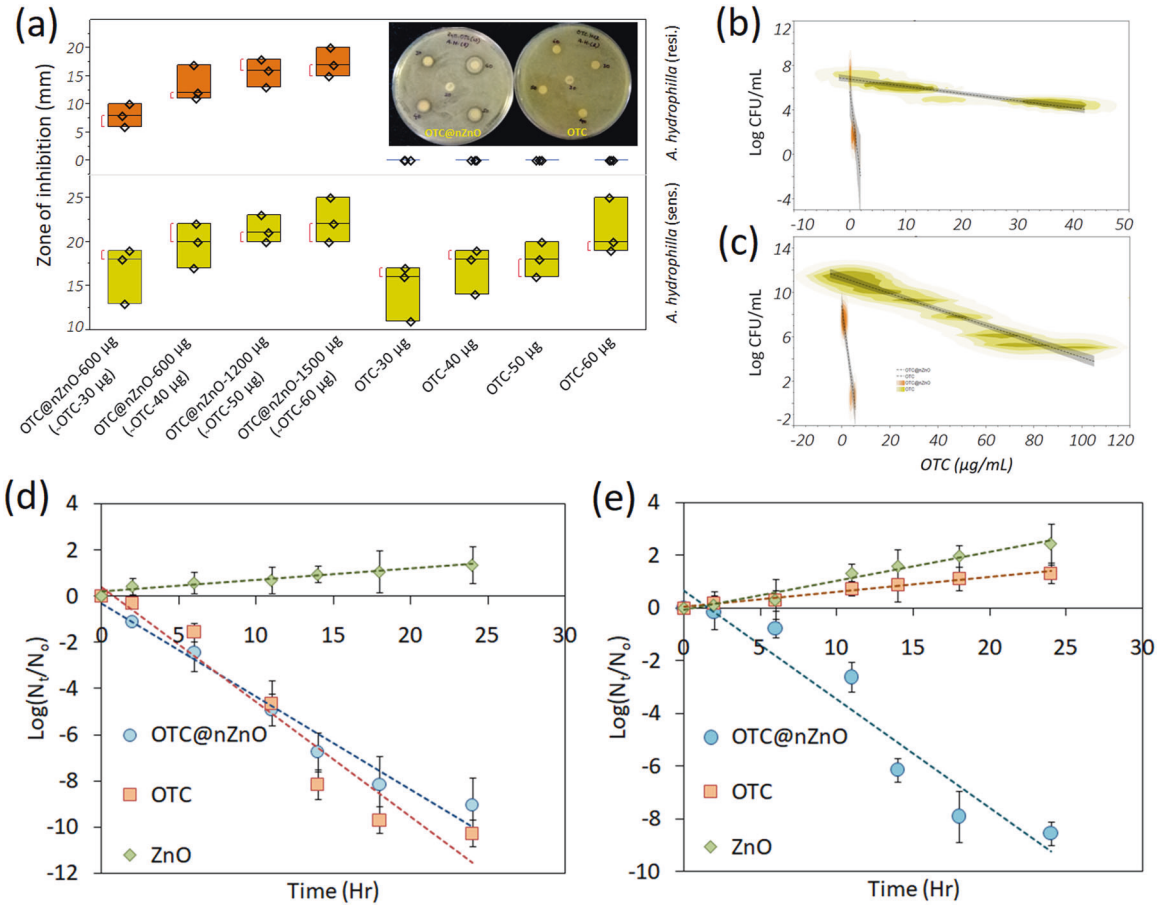

Fig. 3 Antibiogram of OTc and OTc@nZnO against resistant and sensitive strains of *A. hydrophila* (**a**); minimum inhibitory concentration of OTc@nZnO against OTc sensitive (**b**) and resistant strain (**c**) of *A. hydrophilla*; death kinetics in presence 15.5 µg ml^{-1} OTc@ZnO and equivalent concentration of free OTc and free nZnO against sensitive *A. hydrophila* (**d**); and 77.78 µg ml^{-1} OTc@ZnO and equivalent concentration of free OTc and free nZnO against OTc resistant *A. hydrophila* (**e**)

caused gradual decline CFU number for *A. hydrophila* ATCC 7966 strain during 24 h study. However, it could not be able to do the same for the strain CIAHRT_11. Similarl to antibiogram study, free nZnO could not be able to exert any antibacterial efficacy during 24 h study against both the strain. In contrary, OTc@nZnO performed excellent by gradual decline of CFU number for both the strains i.e., ATCC 7966 and CIAHRT_11. According to the first-order kinetic model, Otc@ZnO showed a higher (−1.14) death rate constant for *A. hydrophila* (ATCC 7966) as compared to *A. hydrophila* (CIAHRT_11) (−0.93) (Table 1). This signifies that Otc@nZnO was faster in killing the sensitive strains of *A. hydrophila* as compared to the resistant one. This might due the fact the sustained or delayed release of $[ZnOTc]^{+}$ from the Otc@nZnO. However, interestingly the *D*-value, which signifies the time required to kill 1-log cycle bacterial population, of Otc@nZnO against both the strains are nearly same (2.49 and 2.43, respectively) (Table 1). This fact signifies that the efficacy rate of Otc@nZnO against both the sensitive and resistant strains of *A. hydrophila* were similar. Tc incorporated in calcium phosphate nanoparticles was also reported to kill faster multidrug-resistant bacteria as compared to free Tc [21].

Table 1 Death kinetic parameters of OTc@nZnO against sensitive and resistant strain of *A. hydrophila*

	A. hydrophila (Sensitive)			*A. hydrophila* (Resistant)		
	k	R^2	*D*-value (h)	*k*	R^2	*D*-value (h)
nZnO	1.13	0.94	−2.04	0.25	0.97	−9.17
OTc.HCl	−1.14	0.94	2.02	0.13	0.98	−17.54
OTc@nZnO	−0.93	0.97	2.49	−0.95	0.93	2.43

Molecular docking to resistant proteins

Tc antibiotics like OTc preferably bind to highly conserved 16S rRNA in 30S ribosomal subunit arresting translation by sterically hindering docking of aminoacyl t-RNA [12]. However, the process gets interrupted by the presence of resistance gene encoding TetA efflux protein which transports intracellular Tc out of cell cytoplasm. Further, the

Table 2 Molecular docking simulation results and interaction analysis between resistance proteins and test ligands ($[MgOTc]^+$ and $[ZnOTc]^+$)

Proteins	Ligand	LBE (kcal/mol)	*Ki*	ImE (kcal/mol)	EsE (kcal/mol)	IE (kcal/mol)	TFE (kcal/mol)	Number of H-bonds and bonding residues	Hydrophobic interaction
Tet(R)	$[MgOTc]^+$	−8.45	637.23 nM	−10.24	−0.26	−2.58	+1.79	5 (His^{100}, Asn^{82}, Gln^{116})	Leu^{60} His^{64} Thr^{103}, Pro^{105}, Ala^{113}, Leu^{134}, Gln^{135}, Ser^{138}
	$[ZnOTc]^+$	−5.49	93.95 µM	−10.57	−0.60	−6.84	+5.07	11 (Thr^{103}, His^{100}, $Ser^{138}Asn^{82}$, Gln^{116})	Ser^{104}, Gln^{135}, Phe^{86}, His^{64}, Leu^{134}, Ala^{113}, Pro^{105}
Tet(A)	$[MgOTc]^+$	−8.26	884.8 nM	−10.05	−0.20	−2.56	+1.79	5 (His_{258}, Gln^{222})	Phe^{254}, Leu^{316}, Phe^{138}, Gly^{135}, Ile^{221}, Gly^{312}, Gly^{225}
	$[ZnOTc]^+$	−4.4	0.56 mM	−9.51	−0.25	−7.65	+5.07	7 (Gln^{222}, His^{344}, Gln^{54}, Gly^{108}, Gln^{320})	Leu^{316}, His^{258}, Gly^{135}, Thr^{343}, Tyr^{50}, Phe^{138}

LBE lowest binding energy, *Ki* inhibition constant at 298.15 K, *ImE* intermolecular energy, *EsE* electrostatic energy, *IE* internal energy, *TFE* torsional free energy, *mM* millimolar, *µM* micromolar, *nM* nanomolar

expression of TetA protein is governed by TetR protein which upon binding with Tc lost its regulation over expression of TetA [14]. It was reported that the Tc binding pocket of TetR protein is composed of the COOH-termini of α4 and α6 and the helices α5, α7, α8, α8', and α9' [16]. Tc binds in this pocket in coordination with Mg^{2+} and H-binding with the amino acid residues. The Mg^{2+} forms octahedral coordination with the chelating ketoenolate moiety at O-11/O-12 of Tc, His^{100}Nϵ and three H_2O molecules which further forms H-bond to the carboxylate of Glu^{147}. The residues Gln^{116}NϵH and His^{64}NϵH also forms H bonds to the amide oxygen in position 2 and negatively charged enolate O-3. The O-3 and the positively charged ammonium N-4 forms H-bond to amide chain of Asn^{82}. The hydroxyl at O-121 form aromatic H-bond with Phe^{86}. The aromatic ring D form hydrophobic interaction with Pro^{105}, Leu^{170}, leu^{174}, Met^{177} and Arg^{104} [16]. Hence binding of drug molecule to TetR is very vital in resistance development in bacteria and in the present study the binding characteristics of $[ZnOTc]^+$ toward TetR(E) is evaluated by molecular docking studies with the already reported binding pocket using AutoDock. Though it was reported that binding poses and affinities information obtained from Autodock may not be exact with the experimental finding [44], in the present study it was performed to get an idea on comparative binding properties between two antibacterial compounds. The predicted binding energy of $[MgOTc]^+$ and $[ZnOTc]^+$ for TetR is summarized in Table 2. It was found that the calculated lowest binging energy (LBE) of $[MgOTc]^+$ is low for TetR(E) as compared to $[ZnOTc]^+$. This signifies that the binding affinity of $[ZnOTc]^+$ toward the resistance protein TetR is less as compared to $[MgOTC]^+$. Further, the inhibition constant (*Ki*) of $[ZnOTc]^+$ for TetR(E) was also calculated to be in micromolar range (µM) as compared to nanomolar (nM) for $[MgOTc]^+$. The docking score or LBE indicates a direct relationship between the energy of the binding affinity, referring to the lowest docking scores and stability [59].

The interaction analysis between 5A,6-anhydrotetracycline TetR in PDB ID: 5MRU_A using LigPlot+ revealed that the ligand binds to the specific pocket of TetR with 8 H-bonds with Thr^{103}, His^{100}, Ser^{67}, His^{64} and Asn^{82}; and Hydrophobic interaction with Pro^{105}, Leu^{60}, Leu^{134}, Phe^{86}, Gln^{116}, Ser^{138}, Met^{135} and Arg^{104} (Fig. S6aiii and Table S6). However, in the present study despite the same Tc binding pocket in TetR protein was used for docking studies [16], $[MgOTc]^+$ formed different orientation which might be due to introduction of extra hydroxyl moiety at the 5 position in OTc and change in the amino acid sequence of TetR of *A. hydrophila*. In the present study, Mg^{2+} did formed octahedral coordination but did not participate in binding with any amino acid residue. However, the His^{100} formed H-bond with the hydroxyl group present at O-9 position (Fig. 4aii). Like reported earlier the

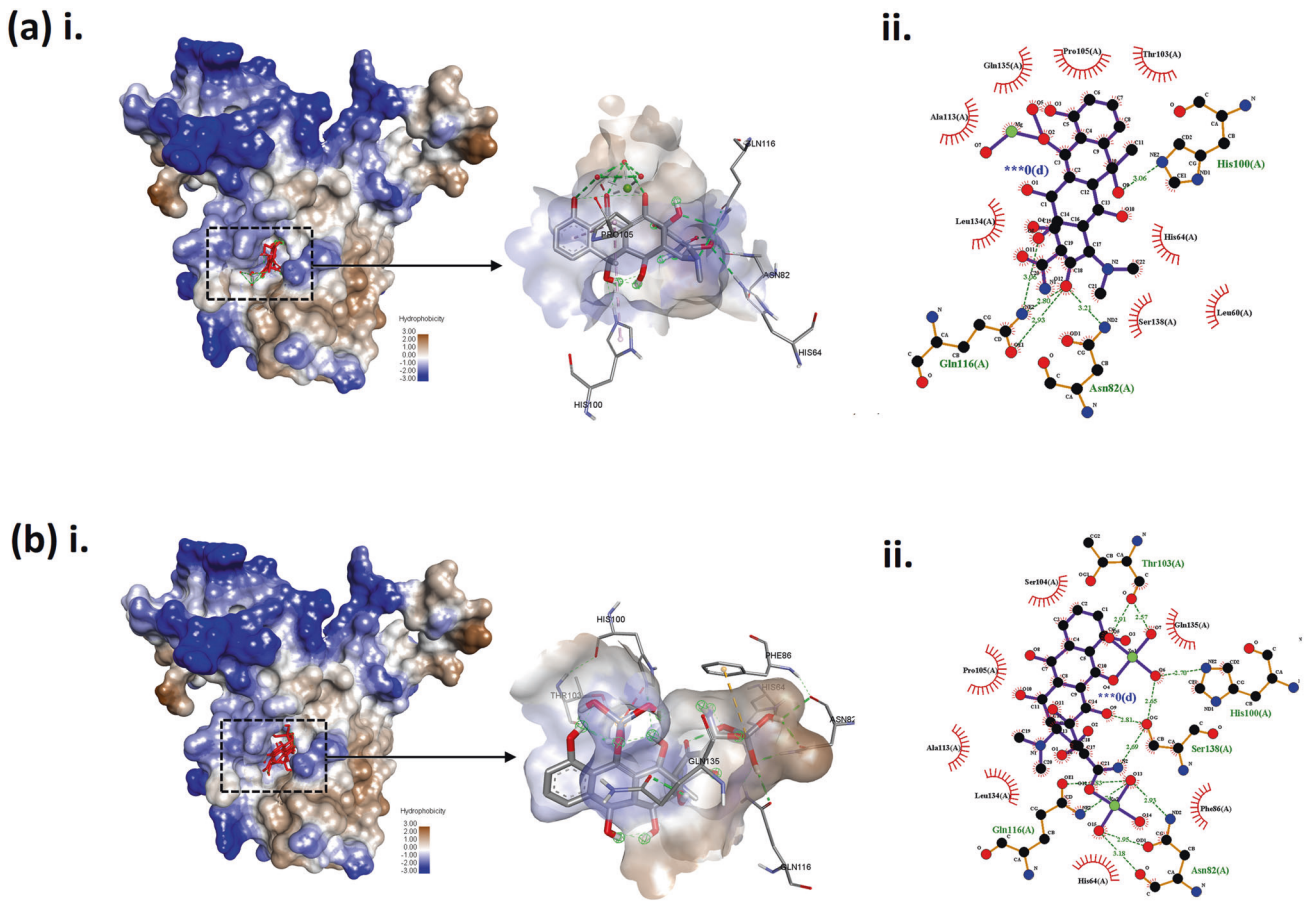

Fig. 4 3D representation (i) and binding mode (ii) of TetR(E) with $[MgOTc]^+$ (**a**) and $[ZnOTc]^+$ (**b**)

residues Gln^{116} did participated actively, however made H-bonds with the O-8 and O-12. The aromatic ring D formed hydrophobic interaction with Pro^{105}, Thr^{103} and Gln^{135} (Fig. 4aii and Table 2). Further, the $[ZnOTc]^+$ also showed different orientation in the same pocket with higher binding energy (LBE, −5.49 Kcal mol^{-1}) (Table 2). The^{103}, His^{100} and Ser^{138} formed 6 H-bonds with Zn-OH, O-9 and N of amide moiety (Fig. 4bii). Due to presence of Zn^{2+} at the amide moiety, Asn^{82} and Gln^{116} formed H-bonds with Zn-OH. The hydrophobic interaction existed between aromatic ring D with Pro^{105}, Ser^{104} and Gln^{135}. Previously, molecular docking with OTc with parental TetR in a different platform (YASARA 16.2.18) reported good binding energy of 9.03 kCal/mol with hydrophobic interaction with five amino acid residues (His^{64}, Phe^{86}, Pro^{105}, Gly^{138} and His^{139}) and pi-pi bond with Phe^{86} [60, 61]. However, in that study OTc intercalation with Mg^{2+} in octahedral complex was not considered for docking purpose. In another study caffeic acid and gallic acid were evaluated for assessing their binding affinity toward TetR of *Streptococcus* spp. using AutoDock 4.2 [43]. Both the acids were reported to have promising inhibitory effect against TetR with binding energy of −5.93 Kcal mol^{-1} and –3.92 Kcal mol^{-1} with 7 and 4 H-bond interactions.

Recently, there are many reports on in silico evaluation of chemical compounds for their inhibitory effects toward antibiotics efflux pumps. For example, MepA efflux pump inhibitory effect of 1,8-naphthyridines sulfonamides was studied using molecular docking techniques against *Staphylococcus aureus* [62]. Further, the same compounds are also evaluated in silico for their inhibitory action against NorA efflux pump [63]. Similarly, anti-fungal azoles compounds were also evaluated for their inhibitory effect toward Tet(K) efflux pump of *Staphylococcus aureus* through simulation studies [64]. Similarly, in silico docking studies (AutoDock Vina) of TetA efflux protein of *E. coli* with berberine and Tc resulted higher free energies of −7.3 and −6.7 kcal/mol, respectively [65]. However, in the present study, the binding efficacy of drug molecules toward TetA(E) efflux protein was done to understand the better antibacterial properties of $[ZnOTc]^+$. The binding affinity of $[ZnOTc]^+$ with TetA(E) efflux protein was calculated using molecular docking and compared with $[MgOTc]^+$. $[MgOTc]^+$ showed higher binding affinity toward TetA(E) with low LBE (−8.26 Kcal/mol) and low *Ki* (nanomolar range). However, $[ZnOTc]^+$ performed poorly in binding the pockets of TetA(E). It was having high LBE (−4.4 Kcal mol^{-1}) and *Ki* constant (millimolar range). Hence

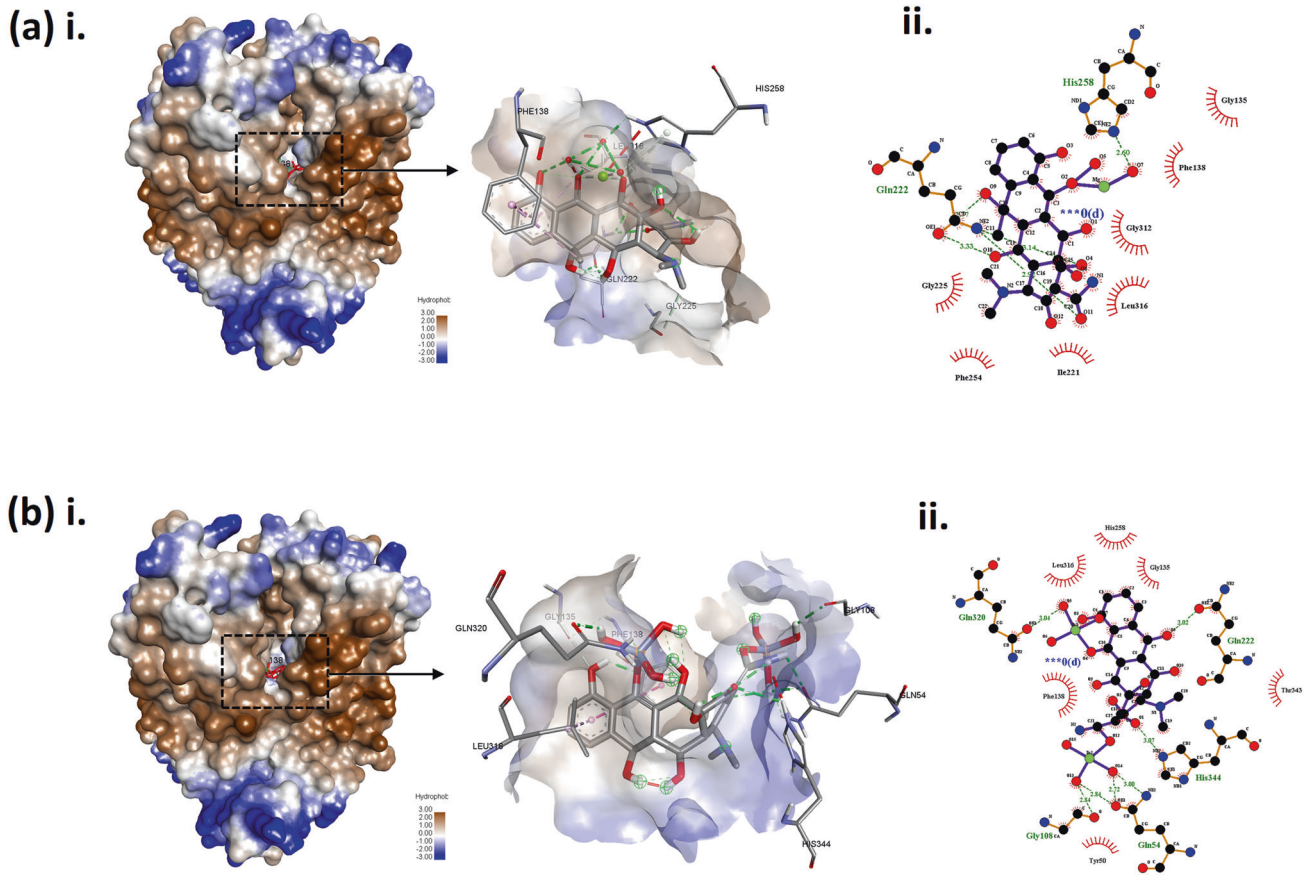

Fig. 5 3D representation (i) and binding mode (ii) of TetA(E) with $[MgOTc]^+$ (**a**) and $[ZnOTc]^+$ (**b**)

it could be postulated that $[ZnOTc]^+$ can effectively bypass the efflux protein as compared to $[MgOTc]^+$ to render the antibacterial activity by binding with 16S rRNA of 30S ribosomal subunit. It was reported that motif A of TetA consisted with $G^{64}ALSD^{68}RFG^{71}R^{72}RP$ is responsible for binding with Tc [65]. In the present study, the $[MgOTc]^+$ was found to bind of TetA(E) with hydrophobic interactions with Phe^{138}, Gly^{135}, Ile^{221}, Gly^{312}, Gly^{225}, Phe^{254}, Leu^{316} and 5 H-bonding with His^{258} and Gln^{222} (Fig. 5aii). However, $[ZnOTc]^+$ only formed 7 H-bond (Gln^{222}, His^{344}, Gln^{54}, Gly^{108}, Gln^{320}) and five hydrophobic interactions (Leu^{316}, His^{258}, Gly^{135}, Thr^{343}, Tyr^{50}) with the amino acid residues of TetA(E) (Fig. 5bii).

Molecular docking to 16s rRNA

The complexation with divalent Mg^{2+} is also crucial for the binding of Tc to acceptor site for aminoacylated tRNA between head and body the 30S ribosomal subunit [66]. Tc binding pocket is formed by H^{34} (RNA residues 1196–1200:1053–1056) in combination with residues 964–967 from the H^{31} stem-loop in *Thermus thermophilus* [6]. It primarily forms H-bonds with the exposed backbone sugar phosphate oxygen atoms of H^{34}. The hydrophobic interaction of Tc happens with the bases of 1054 and 1196 RNA residues. The flat fused-ring structure of Tc molecules with hydrophilic functional groups along one side can make both charged and hydrophobic or interactions. The 30S ribosomal subunit was reported to have three binding sites for binding tRNA viz. A (aminoacyl), P (peptidyl) and E(exit) sites [6]. A general consensus is that Tc particularly blocks binding of aminoacyl-tRNA to the A site of the protein synthesis machinery of mRNA-ribosome complex [67, 68]. However, the exact binding site and mechanism is not fully confirmed [6].

Since binding of drug molecule to the A site of 16S rRNA is necessary to exert its protein inhibition property, molecular docking of $[ZnOTC]^+$ was also performed with 16S rRNAs of both the strains (ATCC 7966 and CIAHRT_11) of *A. hydrophila*. Since crystallographic data of 16s rRNA of *A. hydrophila* is not available we prepared 3-D fold for both the strains using Ab initio technique. It was reported that intercalation of divalent Mg^{2+} is very crucial for binding of Tc to the rRNA [69]. The Mg^{2+} forms salt bridges with phosphate oxygen atoms of G^{1197} and G^{1198}. Further, presence of Mg^{2+} ion in absence of Tc was also reported to maintain local structure of 30S in that region [70]. Hence in the present study docking was

Table 3 Molecular docking simulation results and interaction analysis between 16S rRNA of *A. hydrophila* and test ligands ($[MgOTc]^+$ and $[ZnOTc]^+$)

16S RNAs	Ligand	LBE (kcal/mol)	*Ki*	ImE (kcal/mol)	EsE (kcal/mol)	IE (kcal/mol)	TFE (kcal/mol)	Number of H-bonds and bonding residues
Sensitive (CCM 7232)	$[MgOTc]^+$	−16.27	1.18 pM	−18.06	−10.11	−2.06	+1.79	12 (U^{1121}, G^{1122}, C^{1123}, G^{1238}, A^{1125}, U^{1236})
	$[ZnOTc]^+$	−11.43	4.21 nM	−16.50	−10.17	−8.38	+5.07	8 (U^{312}, A^{348}, G^{332}, C^{347})
Resistant (CIAHRT_11)	$[MgOTc]^+$	−19.10	10.05 fM	−20.89	−13.12	−3.03	+1.79	13 (C^{375}, A^{742}, C^{260}, U^{259}, G^{680}, G^{755})
	$[ZnOTc]^+$	−15.76	2.79 pM	−20.83	−12.87	−8.08	+5.07	10 (U^{386}, G^{387}, A^{803}, A^{377}, C^{802}, U^{738})

LBE lowest binding energy, *Ki* inhibition constant at 298.15 K, *ImE* intermolecular energy, *EsE* electrostatic energy, *IE* internal energy, *TFE* torsional free energy, *nM* nanomolar, *pM* picomolar, *fM* femtomolar

performed Mg intercalated OTc i.e. $[MgOTc]^+$. It binds with rRNA with very low binding energy (−19.10 to −16.27 kcal mol^{-1}) and the *Ki* is also very low (femto to picomolar range) (Table 3). The very low binding energy between $[MgOTc]^+$ and 16S rRNA may explained by formation of many H-bonds. The binding pocket of $[MgOTc]^+$ in 16S rRNA of CCM 7232 consisted of 12 H-bonds with U^{1121}, G^{1122}, C^{1123}, G^{1238}, A^{1125} and U^{1236}; whereas in case of CIAHRT_11 it formed 10 H-bond with U^{386}, G^{387}, A^{803}, A^{377}, C^{802} and U^{738} (Table 3 and Fig. S8). Similarly, $[ZnOTc]^+$ also showed very low binding energy (−15.76 to −11.43 kcal mol^{-1}) with both the 16S rRNAs and the *Ki* of $[ZnOTc]^+$ for both 16S rRNA are found to nano to pico molar range (Table 3). $[ZnOTc]^+$ also formed 8 H-bonds with U^{312}, A^{348}, G^{332} and C^{347} of 16S rRNA of CCM 7232, and 10 H-Bonds with U^{386}, G^{387}, A^{803}, A^{377}, C^{802} and U^{738} (Table 3 and Fig. S8). Hence it could be postulated that besides having low binding affinity toward the Tc resistance proteins, $[ZnOTc]^+$ is also having high binding affinity toward the 16s rRNA thus exerting antibacterial property to resistant microorganism.

Conclusion

The present study describes simple synthesis method of Zn^{2+} intercalated OTc molecules encapsulated in crystal structure of ZnO nanoparticles. The particles were hexagonal in shape with average size of 99 nm. Spectroscopic investigation revealed Zn^{2+} intercalation on the ring structure of OTc at ring A and ring D with respective amide and aromatic carbonyl moieties. In vitro release profile of Zn^{2+} intercalated OTc demonstrated sustained release of nearly 80% loaded OTc over 2 days. Due to nanotization and intercalation of Zn^{2+}, modified OTc molecule showed superior antibacterial properties toward resistant strain of *Aeromonas hydrophila* as compared to free OTc. The minimum inhibitory concentration of free oxytetrcycline was 150 μg ml^{-1} and nanotized Zn^{2+} intercalated oxytetrcycline performed better with very low inhibitory concentration equivalent to 7.02 μg ml^{-1} of OTc. It was also observed that nanotization and Zn^{2+} intercalation also reduced the minimum inhibitory concentration against sensitive strains of *A. hydrophila* with faster cell death kinetics. To understand the mechanism of superior action of nanotized Zn^{2+} intercalated oxytetrcycline, molecular docking was performed that revealed less binding affinity toward Tc resistant proteins i.e. TetR(E) and TetA(E) as compared to free OTc. Molecular docking also revealed that Zn^{2+} intercalated oxytetrcycline had good binding affinity toward 16S rRNA of 30S ribosomal subunit of *A. hydrophila*. Finally, this study suggests that nanotization of OTc through Zn^{2+} intercalation and encapsulation in

ZnO nanoparticles could break the Tc resistance pattern of *A. hydrophila* strains which are causing several fish mortality in aquaculture farm. However, further in vivo studies are required for its feasibility for use in animal health care.

Acknowledgements The authors are highly grateful to the Indian Council of Agricultural Research (ICAR), Government of India for providing financial assistance for carrying out the present research under Institute Project "Fish Health Management and Antimicrobial resistance in Inland Open Waters" (FREM/17–20/14).

Compliance with ethical standards

Conflict of interest The authors declare no competing interests.

References

1. Welling V, Lundeheim N, Bengtsson B. A pilot study in Sweden on efficacy of benzylpenicillin, oxytetracycline, and florfenicol in treatment of acute undifferentiated respiratory disease in calves. Antibiotics. 2020;9:736.
2. Watts KM, Lahiri P, Arrazuria R, De Buck J, Knight CG, Orsel K, Barkema HW, Cobo ER. Oxytetracycline reduces inflammation and treponeme burden whereas vitamin D3 promotes β-defensin expression in bovine infectious digital dermatitis. Cell Tissue Res. 2020;379:337–48.
3. Kumar G, Menanteau-Ledouble S, Saleh M, El-Matbouli M. *Yersinia ruckeri*, the causative agent of enteric redmouth disease in fish. Vet Res. 2015;46:103.
4. Uno K. Pharmacokinetic study of oxytetracycline in healthy and vibriosis-infected ayu (*Plecoglossus altivelis*). Aquaculture. 1996; 143:33–42.
5. Abraham TJ, Sasmal D, Banerjee T. Notes bacterial flora associated with diseased fish and their antibiogram. J Indian Fish Assoc. 2004;31:177–80.
6. Brodersen DE, Clemons WM, Jr, Carter AP, Morgan-Warren RJ, Wimberly BT, Ramakrishnan V. The structural basis for the action of the antibiotics tetracycline, pactamycin, and hygromycin B on the 30S ribosomal subunit. Cell. 2000;103:1143–54.
7. Klima CL, Holman DB, Cook SR, Conrad CC, Ralston BJ, Allan N, Anholt RM, Niu YD, Stanford K, Hannon SJ, Booker CW. Multidrug resistance in *Pasteurellaceae* associated with bovine respiratory disease mortalities in North America from 2011 to 2016. Front Microbiol. 2020;11:606438.
8. Shahbazi P, Nouri Gharajalar S, Mohebbi K, Taeb J, Hashemzadeh Farhang H, Nikvand AA, Norouzi R. First survey on the presence and distribution of oxytetracycline-resistance genes in Anaplasma species. Acta Parasitol. 2021;66:501–7.
9. Dang H, Zhao J, Song L, Chen M, Chang Y. Molecular characterizations of chloramphenicol-and oxytetracycline-resistant bacteria and resistance genes in mariculture waters of China. Mar Pollut Bull. 2009;58:987–94.
10. Dang H, Zhang X, Song L, Chang Y, Yang G. Molecular determination of oxytetracycline-resistant bacteria and their resistance genes from mariculture environments of China. J Appl Microbiol. 2007;103:2580–92.
11. Dang H, Zhang X, Song L, Chang Y, Yang G. Molecular characterizations of oxytetracycline resistant bacteria and their resistance genes from mariculture waters of China. Mar Pollut Bull. 2006;52:1494–503.
12. Grossman TH. Tetracycline antibiotics and resistance. Cold Spring Harb Perspect Med. 2016;6:a025387.
13. Chopra I, Roberts M. Tetracycline antibiotics: mode of action, applications, molecular biology, and epidemiology of bacterial resistance. Microbiol Mol Biol Rev. 2001;65:232–60.
14. Kisker C, Hinrichs W, Tovar K, Hillen W, Saenger W. The complex formed between tet repressor and tetracycline-Mg^{2l} $^{ihsbopl+}$ reveals mechanism of antibiotic resistance. J Mol Biol. 1995;247: 260–80.
15. Takahashi M, Altschmied L, Hillen W. Kinetic and equilibrium characterization of the tet repressor-tetracycline complex by fluorescence measurements: evidence for divalent metal ion requirement and energy transfer. J Mol Biol. 1986;187:341–8.
16. Hinrichs W, Kisker C, Düvel M, Müller A, Tovar K, Hillen W, Saenger W. Structure of the Tet repressor-tetracycline complex and regulation of antibiotic resistance. Science. 1994;264:418–20.
17. Dias AM, da Silva FG, de Figueiredo Monteiro AP, Pinzón-García AD, Sinisterra RD, Cortés ME. Polycaprolactone nanofibers loaded oxytetracycline hydrochloride and zinc oxide for treatment of periodontal disease. Mater Sci Eng C. 2019;103:109798.
18. De Oliveira DM, Forde BM, Phan MD, Steiner B, Zhang B, Zuegg J, El-Deeb IM, Li G, Keller N, Brouwer S, Harbison-Price N. Rescuing tetracycline class antibiotics for the treatment of multidrug-resistant *Acinetobacter baumannii* pulmonary infection. MBio. 2022;13:e03517–21.
19. Huh AJ, Kwon YJ. "Nanoantibiotics": a new paradigm for treating infectious diseases using nanomaterials in the antibiotics resistant era. J Control Release. 2011;156:128–45.
20. Ghosh D, Chandra S, Chakraborty A, Ghosh SK, Pramanik P. A novel graphene oxide-para amino benzoic acid nanosheet as effective drug delivery system to treat drug resistant bacteria. Int J Pharm Sci Drug Res. 2010;2:127–33.
21. Mukherjee R, Patra M, Dutta D, Banik M, Basu T. Tetracycline-loaded calcium phosphate nanoparticle (Tet-CPNP): rejuvenation of an obsolete antibiotic to further action. Biochim Biophys Acta Gen Subj. 2016;1860:1929–41.
22. Assali M, Zaid AN, Abdallah F, Almasri M, Khayyat R. Single-walled carbon nanotubes-ciprofloxacin nanoantibiotic: strategy to improve ciprofloxacin antibacterial activity. Int J Nanomed. 2017;12:6647.
23. Carver JA, Simpson AL, Rathi RP, Normil N, Lee AG, Force MD, Fiocca KA, Maley CE, DiJoseph KM, Goldstein AL, Attari AA. Functionalized single-walled carbon nanotubes and nanographene oxide to overcome antibiotic resistance in tetracycline-resistant *Escherichia coli*. ACS Appl Nano Mater. 2020;3:3910–21.
24. Lin L, Sun L, Ali F, Guo Z, Zhang L, Lin W, Lin X. Proteomic analysis of alterations in *Aeromonas hydrophila* outer membrane proteins in response to oxytetracycline stress. Micro Drug Resist. 2018;24:1067–74.
25. Li W, Zhao Y, Yu J, Lin L, Ramanathan S, Wang G, Lin X, Pang H. TonB-dependent receptors affect the spontaneous oxytetracycline resistance evolution in *Aeromonas hydrophila*. J Proteome Res. 2020;20:154–63.
26. Scarano C, Piras F, Virdis S, Ziino G, Nuvoloni R, Dalmasso A, De Santis EP, Spanu C. Antibiotic resistance of *Aeromonas* ssp. strains isolated from Sparus aurata reared in Italian mariculture farms. Int J Food Microbiol. 2018;284:91–7.
27. Syrova E, Kohoutova L, Dolejska M, Papezikova I, Kutilova I, Cizek A, Navratil S, Minarova H, Palikova M. Antibiotic resistance and virulence factors in mesophilic *Aeromonas* spp. from Czech carp fisheries. J Appl Microbiol. 2018;125:1702–13.
28. Venu Gopal VR, Kamila S. Effect of temperature on the morphology of ZnO nanoparticles: a comparative study. Appl Nanosci. 2017;7:75–82.
29. Sarkar DJ, Sarkar SD, Das BK, Manna RK, Behera BK, Samanta S. Spatial distribution of meso and microplastics in the sediments of river Ganga at eastern India. Sci Total Environ. 2019;694:133712.

30. Korst JJ, Johnston JD, Butler K, Bianco EJ, Conover LH, Woodward RB. The total synthesis of dl-6-demethyl-6-deoxytetracycline. J Am Chem Soc. 1968;90:439–57.
31. Muxfeldt H, Hardtmann G, Kathawala F, Vedejs E, Mooberry JB. Tetracyclines. VII. Total synthesis of dl-terramycin. J Am Chem Soc. 1968;90:6534–6.
32. de Moura Ferraz LR, Tabosa AÉ, da Silva Nascimento DD, Ferreira AS, de Albuquerque Wanderley Sales V, Silva JY, Júnior SA, Rolim LA, de Souza Pereira JJ, Rolim-Neto PJ. ZIF-8 as a promising drug delivery system for benznidazole: development, characterization, in vitro dialysis release and cytotoxicity. Sci Rep. 2020;10:1–4.
33. Parvekar P, Palaskar J, Metgud S, Maria R, Dutta S. The minimum inhibitory concentration (MIC) and minimum bactericidal concentration (MBC) of silver nanoparticles against *Staphylococcus aureus*. Biomater Investig Dent. 2020;7:105–9.
34. Holdsworth SD, Simpson R. Kinetics of microbial death and factors for quality attributes. In: Barbosa-Cánovas GV, editor. Thermal processing of packaged foods. Cham: Springer; 2016. pp. 89–124.
35. Gogoi A, Anki Reddy K, Senthilmurugan S, Kumar, Mondal P. Dehydration of acetic acid using layered graphene oxide (GO) membrane through forward osmosis (FO) process: a molecular dynamics study. Mol Simul. 2020;46:1500–8.
36. Boyd PG, Moosavi SM, Witman M, Smit B. Force-field prediction of materials properties in metal-organic frameworks. J Phys Chem Lett. 2017;8:357–63.
37. Werten S, Schneider J, Palm GJ, Hinrichs W. Modular organisation of inducer recognition and allostery in the tetracycline repressor. FEBS J. 2016;283:2102–14.
38. Webb B, Sali A. Protein structure modeling with MODELLER. Methods Mol Biol. 2014;1137:1–15.
39. Ain-Ali QU, Mushtaq N, Amir R, Gul A, Tahir M, Munir F. Genome-wide promoter analysis, homology modeling and protein interaction network of dehydration responsive element binding (DREB) gene family in *Solanum tuberosum*. PLoS ONE. 2021; 16:e0261215.
40. Zuker M. Mfold web server for nucleic acid folding and hybridization prediction. Nucleic Acids Res. 2003;31:3406–15.
41. Wang J, Wang J, Huang Y, Xiao Y. 3dRNA v2. 0: an updated web server for RNA 3D structure prediction. Int J Mol Sci. 2019;20:4116.
42. Wang J, Mao K, Zhao Y, Zeng C, Xiang J, Zhang Y, Xiao Y. Optimization of RNA 3D structure prediction using evolutionary restraints of nucleotide–nucleotide interactions from direct coupling analysis. Nucleic Acids Res. 2017;45:6299–309.
43. Sivakumar S, Girija AS, Priyadharsini JV. Evaluation of the inhibitory effect of caffeic acid and gallic acid on tetR and tetM efflux pumps mediating tetracycline resistance in *Streptococcus* sp., using computational approach. J King Saud Univ Sci. 2020; 32:904–9.
44. Plewczynski D, Łaźniewski M, Augustyniak R, Ginalski K. Can we trust docking results? Evaluation of seven commonly used programs on PDBbind database. J Comput Chem. 2011;32: 742–55.
45. Laskowski RA, Swindells MB. LigPlot+: multiple ligand–protein interaction diagrams for drug discovery. J Chem Inf Model. 2011; 51:2778–86.
46. Odorici G, Monfrecola G, Bettoli V. Tetracyclines and photosensitive skin reactions: a narrative review. Dermatol Ther. 2021; 34:e14978.
47. Goswami M, Adhikary NC, Bhattacharjee S. Effect of annealing temperatures on the structural and optical properties of zinc oxide nanoparticles prepared by chemical precipitation method. Optik. 2018;158:1006–15.
48. Khanom S, Hayashi N. Removal of metal ions from water using oxygen plasma. Sci Rep. 2021;11:1–8.
49. Srivastava OK, Secco EA. Studies on metal hydroxy compounds. II. Infrared spectra of zinc derivatives ε-$Zn(OH)_2$, β-ZnOHCl, ZnOHF, $Zn_5(OH)_8Cl_2$, and $Zn_5(OH)_8Cl_2$. H_2O. Can J Chem. 1967;45:585–8.
50. Rakshit S, Elzinga EJ, Datta R, Sarkar D. In situ attenuated total reflectance Fourier-transform infrared study of oxytetracycline sorption on magnetite. J Environ Qual. 2013;42:822–7.
51. Li Z, Kolb VM, Jiang WT, Hong H. FTIR and XRD investigations of tetracycline intercalation in smectites. Clays Clay Min. 2010;58:462–74.
52. dos Santos Ferreira da Silva J, López Malo D, Anceski Bataglion G, Nogueira Eberlin M, Machado Ronconi C, Alves Júnior S, de Sá GF. Adsorption in a fixed-bed column and stability of the antibiotic oxytetracycline supported on Zn (II)-[2-methylimidazolate] frameworks in aqueous media. PLoS ONE. 2015;10:e0128436.
53. Dev RK, Mishra P, Kumar Chaudhary N, Bhattarai A. Synthesis, characterization, and antibacterial evaluation of heteroleptic oxytetracycline-salicylaldehyde complexes. J Chem. 2020;2020: 7961345.
54. Wellens S, Vander Hoogerstraete T, Möller C, Thijs B, Luyten J, Binnemans K. Dissolution of metal oxides in an acid-saturated ionic liquid solution and investigation of the back-extraction behaviour to the aqueous phase. Hydrometallurgy. 2014;144:27–33.
55. Cardoso D, Narcy A, Durosoy S, Bordes C, Chevalier Y. Dissolution kinetics of zinc oxide and its relationship with physicochemical characteristics. Powder Technol. 2021;378:746–59.
56. Yang Q, Qi H, Lue A, Hu K, Cheng G, Zhang L. Role of sodium zincate on cellulose dissolution in NaOH/urea aqueous solution at low temperature. Carbohyd Polym. 2011;83:1185–91.
57. Thomas R, Jishma P, Snigdha S, Soumya KR, Mathew J, Radhakrishnan EK. Enhanced antimicrobial efficacy of biosynthesized silver nanoparticle based antibiotic conjugates. Inorg Chem Commun. 2020;117:107978.
58. Roshmi T, Soumya KR, Jyothis M, Radhakrishnan EK. Effect of biofabricated gold nanoparticle-based antibiotic conjugates on minimum inhibitory concentration of bacterial isolates of clinical origin. Gold Bull. 2015;48:63–71.
59. Pantsar T, Poso A. Binding affinity via docking: fact and fiction. Molecules. 2018;23:1899.
60. Wang G, Zhang HC, Liu J, Wang JP. A receptor-based chemiluminescence enzyme linked immunosorbent assay for determination of tetracyclines in milk. Anal Biochem. 2019;564:40–6.
61. Wang G, Xia WQ, Liu JX, Wang JP, Liu J. Directional evolution of TetR protein and development of a fluoroimmunoassay for screening of tetracyclines in egg. Microchem J. 2019;150:104184.
62. de Morais Oliveira-Tintino CD, Tintino SR, Muniz DF, dos Santos Barbosa CR, Pereira RL, Begnini IM, Rebelo RA, da Silva LE, Mireski SL, Nasato MC, Krautler MI. Chemical synthesis, molecular docking and MepA efflux pump inhibitory effect by 1, 8-naphthyridines sulfonamides. Eur J Pharm Sci. 2021;160:105753.
63. de Morais Oliveira-Tintino CD, Muniz DF, dos Santos Barbosa CR, Pereira RL, Begnini IM, Rebelo RA, da Silva LE, Mireski SL, Nasato MC, Krautler MI, Pereira PS. The 1, 8-naphthyridines sulfonamides are NorA efflux pump inhibitors. J Glob Antimicrob Resist. 2021;24:233–40.
64. Mahey N, Tambat R, Verma DK, Chandal N, Thakur KG, Nandanwar H. Antifungal azoles as tetracycline resistance modifiers in *Staphylococcus aureus*. Appl Environ Microbiol. 2021;87:e00155–21.
65. Li Y, Cao ZT, Wang XY, Ge XZ. Expression of the TetA gene encoding TetA efflux protein in *E. coli* contributes to its increased bacterial resistance toward berberine. J Asian Nat Prod Res. 2018; 20:374–84.

66. Ross JI, Eady EA, Cove JH, Cunliffe WJ. 16S rRNA mutation associated with tetracycline resistance in a gram-positive bacterium. Antimicrob Agents Chemother. 1998;42:1702–5.
67. Geigenmüller U, Nierhaus KH. Tetracycline can inhibit tRNA binding to the ribosomal P site as well as to the A site. Eur J Biochem. 1986;161:723–6.
68. Maxwell IH. Partial removal of bound transfer RNA from polysomes engaged in protein synthesis in vitro after addition of tetracycline. Biochim Biophys Acta Nucleic Acids Protein Synth. 1967;138:337–46.
69. White JP, Cantor CR. Role of magnesium in the binding of tetracycline to *Escherichia coli* ribosomes. J Mol Biol. 1971; 58:397–400.
70. Carter AP, Clemons WM, Brodersen DE, Morgan-Warren RJ, Wimberly BT, Ramakrishnan V. Functional insights from the structure of the 30S ribosomal subunit and its interactions with antibiotics. Nature. 2000;407:340–8.